Journal of Materials Chemistry C

PAPER

View Article Online
View Journal | View Issue

Cite this: J. Mater. Chem. C, 2014, 2, 9149

Controlled synthesis and tunable luminescence of uniform $YPO_4 \cdot 0.8H_2O$ and $YPO_4 \cdot 0.8H_2O : Tb^{3+}$/$Eu^{3+}$ nanocrystals by a facile approach†

Lei Zhang,[a] Linlin Fu,[a] Xingxing Yang,[a] Zuoling Fu,*[a] Xiangdong Qi[c] and Zhijian Wu[b]

Uniform and well-crystallized $YPO_4 \cdot 0.8H_2O$ and $YPO_4 \cdot 0.8H_2O : Tb^{3+}$, Eu^{3+} nanocrystals have been successfully synthesized by a facile hydrothermal method using trisodium citrate (Cit^{3-}) as a "shape modifier". X-ray diffraction (XRD), field emission-scanning electron microscopy (FE-SEM), high-resolution transmission electron microscopy (HRTEM) and photoluminescence (PL) spectra were used to characterize the samples. It was found that the pH of the initial solution was responsible for determining the shape of the final products. In addition, the $YPO_4 \cdot 0.8H_2O$ samples prepared by Cit^{3-}-assisted hydrothermal synthesis exhibited an intense and bright blue emission. Characterized with Fourier transform infrared (FT-IR) spectra and electron paramagnetic resonance (EPR) spectra, the carbon-related impurities induced by trisodium citrate (Cit^{3-}) in the hydrothermal process were confirmed and confirmed that the paramagnetic defects relating to the luminescence properties existed in the luminescent $YPO_4 \cdot 0.8H_2O$ nanocrystals. More interestingly, the $YPO_4 \cdot 0.8H_2O : Tb^{3+}$, Eu^{3+} samples could be effectively excited with 380 nm and the luminescence colors of $YPO_4 \cdot 0.8H_2O : Tb^{3+}$, Eu^{3+} nanocrystals can be easily tuned by changing the concentration of Eu^{3+} ions due to an efficient energy transfer from Tb^{3+} to Eu^{3+}. These results revealed that the combination of the defect luminescence and rare earth-doping emission in $YPO_4 \cdot 0.8H_2O : Tb^{3+}$, Eu^{3+} nanocrystals could result in tunable emission in a large color gamut, which may be potentially applied in fields such as solid state lighting and field emission displays.

Received 3rd July 2014
Accepted 13th September 2014

DOI: 10.1039/c4tc01427h

www.rsc.org/MaterialsC

1. Introduction

In recent years, inorganic luminescent materials/phosphors have played a key role in applications such as lighting (*e.g.*, fluorescent tubes and LEDs), displays (*e.g.*, cathode tube displays and field emission displays), imaging (computed tomography), *etc.*[1–4] The current attention on energy saving and green concerns gives a boost to the development of LEDs for lighting because of their advantages of high efficiency, compactness, long operational lifetime, and environmental friendliness.[2,3] Rare earth luminescent materials have attracted significant attention from scientists, due to their unique electronic, optical, and chemical properties resulting from the 4f shell of the ions, and were extensively applied to high-performance magnets, luminescence devices, displays, biolabeling, optical imaging, or phototherapy, *etc.*[4,5] It is well-known that the intrinsic properties of inorganic materials are determined by their sizes, shapes, morphologies, compositions, and crystallinity.[6,7] Thus, the further explorations of well-controlled shapes and novel structures of inorganic rare earth luminescent materials have become an important research topic for synthetic inorganic chemists.

To date, considerable efforts have been devoted to design inorganic nanomaterials with well-defined sizes, shapes, and crystallinity such as lanthanide hydroxide nanowires/nanorods, nanotubes, nanosheets,[8–11] lanthanide orthophosphate nanocrystals,[12–15] nanowires/nanorods[16–19] and nanofibers.[20] Nowadays, it is widely accepted that one of the promising and popular strategies of shape and size control is to carefully select an appropriate organic additive with functional groups that selectively adhere to a particular crystal facet and lead to the morphological modification of the crystals.[21] Among a variety of organic additives, trisodium citrate (labeled as Cit^{3-}) is one of the most common and important organic molecules that has been used extensively as the stabilizer and structure-directing agent to control the nucleation, growth and alignment of crystals.[22,23] For instance, Qian and co-workers reported the effects of Cit^{3-} on Co nanowires[24] and doughnut-shaped ZnO

[a]State Key Laboratory of Super-hard Materials, College of Physics, Jilin University, Changchun 130012, China. E-mail: zlfu@jlu.edu.cn; Fax: +86-431-85167966; Tel: +86-431-85167966

[b]State Key Laboratory of Rare Earth Resources Utilization, Changchun Institute of Applied Chemistry, Chinese Academy of Sciences, Changchun 130022, China

[c]Changchun Institute of Optics, Fine Mechanics and Physics, Chinese Academy of Sciences, Changchun 130033, China

† Electronic supplementary information (ESI) available: Additional graphics as described in the text. See DOI: 10.1039/c4tc01427h

microparticles.[25] Moreover, trisodium citrate effects the luminescence of materials in addition to being a "shape modifier".

$LnPO_4$ (Ln = Y, La, Gd, Lu) has high thermal and chemical stability[26] because Ln^{3+} has an empty, half-filled or fully filled 4f electron shell with a stable structure. $LnPO_4$ (Ln^{3+} = Y, La, Gd, Lu) is suggested to be an excellent host for luminescent materials. In recent years, $LnPO_4$ compounds (Ln = Y, La, Gd, Lu) have been extensively investigated.[16–18] Hasse and co-workers obtained $LnPO_4$ nanocrystal dispersions with good optical properties using a surfactant-assisted route.[27] Feldmann and coworkers synthesized luminescent $LaPO_4 : Ce^{3+}$, Tb^{3+} nanoparticles with a high quantum yield using a microwave-assisted synthesis method using ionic liquids as the reaction media.[28] However, there are still few reports on the synthesis and luminescent properties of $YPO_4 \cdot 0.8H_2O$ nanocrystals. In this work, we chose to synthesize Tb^{3+}/Eu^{3+}-doped $YPO_4 \cdot 0.8H_2O$ nanocrystals for two specific reasons. On the one hand, we attempted to control the size, morphology, and crystallinity of $YPO_4 \cdot 0.8H_2O$ nanocrystals by the use of an organic additive (Cit^{3-}) *via* the hydrothermal process and analyse the mechanism of luminescence. On the other hand, Tb^{3+} and Eu^{3+} in some crystalline modifications of orthophosphates were excellent green and red light emitting centers, respectively. The luminescent properties of Eu^{3+}, Tb^{3+}-codoped $YPO_4 \cdot 0.8H_2O$ phosphors were investigated in detail, and energy transfer mechanism between rare earth ions was also discussed.

2. Experimental details

2.1 Preparation of Eu^{3+}/Tb^{3+}-doped $YPO_4 \cdot 0.8H_2O$ nanocrystals

Materials. Lanthanum oxide, terbium oxide and europium oxide (all 99.99%) were used as starting raw materials. All the other chemicals were analytical grade and were used without further purification. Rare earth nitrate ($Tb(NO_3)_3$ and $Eu(NO_3)_3$) stock solutions of 0.1 M and 0.2 M, respectively, were prepared by dissolving Eu_2O_3 and Tb_4O_7 in concentrated HNO_3 at elevated temperature. Yttrium nitrate hexahydrate ($Y(NO_3)_3 \cdot 6H_2O$) and sodium phosphate (Na_3PO_4) were used as the yttrium source and phosphate source, respectively. Meanwhile, trisodium citrate (A. R.) was used as the "shape modifier".

Synthesis. In a typical procedure, 2 mmol $Y(NO_3)_3 \cdot 6H_2O$ was added to 20 mL of an aqueous solution containing 2 mmol of trisodium citrate (Cit^{3-}) to form the Y^{3+}–Cit^{3-} complex (1 : 1 molar ratio for Cit^{3-}/Y^{3+}). After vigorous stirring for 30 min, 2 mmol of Na_3PO_4 was added into the abovementioned solution. The pH of the mixture was adjusted to a specific value by adding NaOH solution (3 M) or HNO_3 (1 M) solution. After additional agitation for 15 min, the as-obtained mixing solution was transferred into a Teflon bottle held in a stainless steel autoclave, sealed and maintained at 180 °C for 24 h. As the autoclave cooled to room temperature naturally, the precipitates were separated by centrifugation, sequentially washed with deionized water and ethanol, and then dried in air at 60 °C for 12 h. Finally, uniformly distributed spherical $Y_{0.96}PO_4 \cdot 0.8H_2O : 0.04Tb^{3+}$ nanocrystals were obtained. The experiment was repeated under similar conditions for the synthesis of $Y_{(0.96-x)}$ $PO_4 \cdot 0.8H_2O : 0.04$ Tb^{3+}, xEu^{3+}.

2.2 Characterization

X-ray powder diffraction (XRD) measurements were performed on a Rigaku-Dmax 2500 diffractometer at a scanning rate of 15° min^{-1} in the 2θ range from 10° to 65° with graphite monochromatized Cu Kα radiation (λ = 0.15405 nm). The morphology and size of the obtained samples were examined by a field emission-scanning electron microscope (FE-SEM, XL30, Philips) and high-resolution transmission electron microscopy (HR-TEM). The ultraviolet-visible photoluminescence (PL) excitation and emission spectra were recorded with a Hitachi F-7000 spectrophotometer equipped with a Xe-lamp as an excitation source. Fourier transform infrared (FT-IR) spectrum was obtained with a Perkin-Elmer 580B infrared spectrophotometer with the KBr pellet technique. Electron paramagnetic resonance (EPR) spectra were obtained on a JES-FA 200 EPR spectrometer. Luminescent dynamics were investigated using a three part laser system consisting of a (i) Nd:YAG pumping laser (1064 nm), (ii) third-order harmonic generator (blue laser at 486 nm), and (iii) tunable optical parametric oscillator (OPO, Continuum Precision II 8000) with a pulse duration of 10 ns, repetition frequency of 10 Hz, and a line width of 4–7 cm^{-1}. All the measurements were performed at room temperature.

3. Results and discussion

3.1 Phase identification and morphologies

The composition and phase purity of the as-prepared powder samples were first examined by XRD. Different pH values for the synthesis of single phase $YPO_4 \cdot 0.8H_2O$ nanocrystals were investigated by varying the base or acid (NaOH or HNO_3) concentration used in the reaction system. Fig. 1(a)–(g) presented the XRD patterns of the prepared $YPO_4 \cdot 0.8H_2O$ samples at different pH values from 6 to 12. No impurity lines were observed and all the diffraction peaks can be indexed to the pure hexagonal phase of hydrated YPO_4 samples. Fig. 2 shows representative X-ray diffraction patterns of the $YPO_4 \cdot 0.8H_2O$ (a); $YPO_4 \cdot 0.8H_2O : Tb^{3+}$ (b); $YPO_4 \cdot 0.8H_2O : Eu^{3+}$ (c); $YPO_4 \cdot 0.8H_2O : Eu^{3+}$, Tb^{3+} (d) samples. All the diffraction peaks can be readily indexed to pure hexagonal phase according to the JCPDS file no. 42-0028. No obvious shifting of peaks or second phase can be detected at current doping level, indicating that the Tb^{3+} and Eu^{3+} ions were completely dissolved in the $YPO_4 \cdot 0.8H_2O$ host lattice by substituting Y^{3+}. It is also observed that the XRD patterns in Fig. 2(b)–(d) show broad diffraction peaks such that $YPO_4 \cdot 0.8H_2O : Eu^{3+}$, Tb^{3+} particles with nanometer size could form.

The FE-SEM and TEM images provide direct information regarding the size and typical shapes of the as-synthesized $YPO_4 \cdot 0.8H_2O$ samples grown under different experimental conditions. Fig. 3 illustrated the representative FE-SEM and TEM images of the samples prepared at different pH values. The representative panoramic FE-SEM images shown in Fig. 3(a) and (b) demonstrated that the product was composed of a

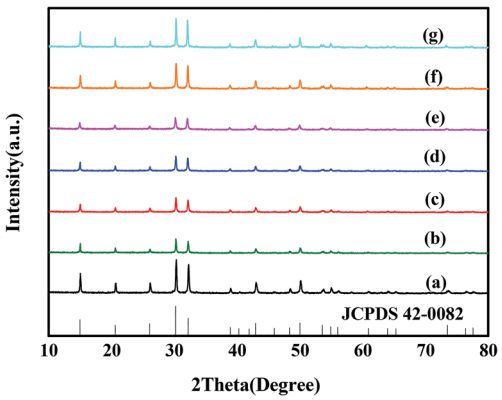

Fig. 1 XRD powder patterns of $YPO_4 \cdot 0.8H_2O$ nanocrystals prepared by the hydrothermal method at 180 °C for 24 h at (a) pH = 6; (b) pH = 7; (c) pH = 8; (d) pH = 9 (e) pH = 10; (f) pH = 11; (g) pH = 12.

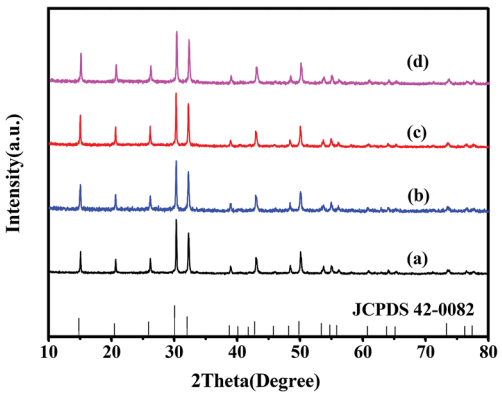

Fig. 2 XRD powder patterns of $YPO_4 \cdot 0.8H_2O$ with different rare earth ions. (a) $YPO_4 \cdot 0.8H_2O$; (b) $YPO_4 \cdot 0.8H_2O : Tb^{3+}$; (c) $YPO_4 \cdot 0.8H_2O : Eu^{3+}$; (d) $YPO_4 \cdot 0.8H_2O : Eu^{3+}, Tb^{3+}$. These samples were prepared under similar conditions. The standard data for $YPO_4 \cdot 0.8H_2O$ (JCPDS card no. 42-0082) is shown as reference.

significant amount of hexagonal nanoprisms with 120 nm in diameter and 130 nm in length at pH = 6. Moreover, the hexagonal nanoprisms were uniformly distributed, and the crystallographic facets were very smooth and clear. When the pH of the initial solution was increased to 11 using NaOH (3 M), the spherical-like nanoparticles were produced, as shown in Fig. 3(c) and (d). However, we can see that the well-defined crystallographic facets of hexagonal prisms were not very evident, and a small quantity of spherical-like particles can also be observed. Furthermore, the surfaces of the crystals were very coarse with some smaller nanoparticles attached on them. These results strongly demonstrated that different pH values of the precursor showed a large impact on the morphologies and nanostructures of $YPO_4 \cdot 0.8H_2O$, and increase in the pH value will make the particles uneven. Therefore, a crystallization pH value of 6 was optimal. Moreover, it is reasonable to show the TEM and HR-TEM images at pH = 6 in Fig. 3(e) and (f). From Fig. 3(e), regular hexagonal cross-section can be seen that corresponded to individual hexagonal prism lying flat on the bottom face parallel to the substrate. The HR-TEM image

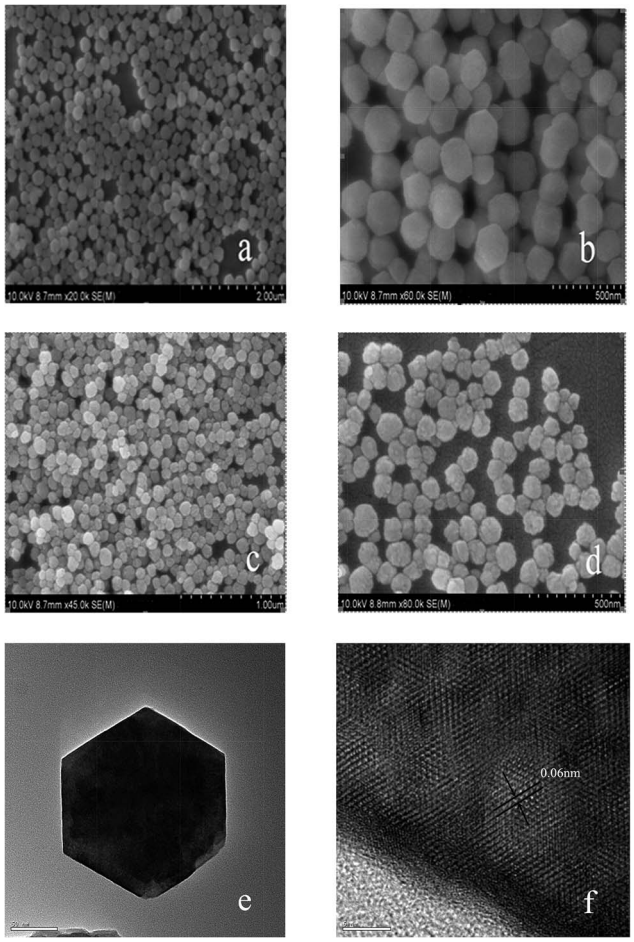

Fig. 3 FE-SEM (a and b) pH = 6; (c and d) pH = 11, TEM (e, pH = 6) and HR-TEM (f, pH = 6) images of $YPO_4 \cdot 0.8H_2O$ samples.

(Fig. 3(f)) showed that the as-obtained crystals were highly crystalline and that the lattice spacing was determined to be ~0.06 nm.

3.2 Luminescence of $YPO_4 \cdot 0.8H_2O$ nanocrystals

Under UV-light irradiation, the $YPO_4 \cdot 0.8H_2O$ nanocrystals exhibited a strong blue emission. Fig. 4 showed the excitation and emission spectra of the as-prepared $YPO_4 \cdot 0.8H_2O$ in the synthesis process. From Fig. 4, we can see that the $YPO_4 \cdot 0.8H_2O$ with Cit^{3-} sample showed a strong emission consisting of a broad band (380–500 nm) with a maximum at 400 nm, and the corresponding excitation spectrum included two broad bands: a weak band from 200 to 240 nm and a strong broad band from 320 to 400 nm with a maximum at 369 nm. In addition, the control experiment without Cit^{3-} in the preparation was also performed. The as-obtained $YPO_4 \cdot 0.8H_2O$ sample in the absence of Cit^{3-} showed no luminescence, the dashed line presented in Fig. 4, indicating that trisodium citrate was the key factor causing blue luminescence. Because neither the Y^{3+} nor the PO_4^{3-} group can show luminescence,[29,30] and the only difference in the hydrothermal process between the luminescent samples and non-luminescent samples is that the former

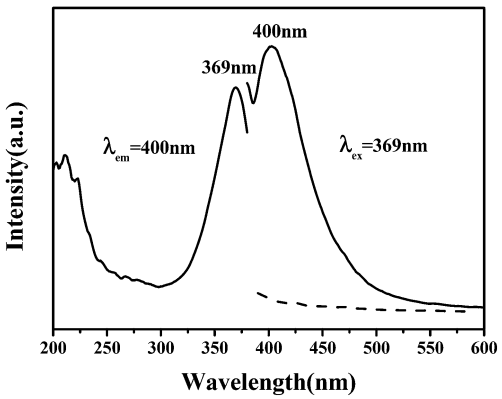

Fig. 4 Excitation and emission spectra of $YPO_4 \cdot 0.8H_2O$ nanocrystals prepared in the presence of trisodium citrate (dashed line is the emission spectrum of $YPO_4 \cdot 0.8H_2O$ nanocrystals prepared without trisodium citrate).

has trisodium citrate as additives while the latter does not; therefore, the observed blue luminescence from $YPO_4 \cdot 0.8H_2O$ sample may be related to some impurities and/or defects in the host lattice. To explore the luminescent mechanism, EPR spectroscopy on the luminescent $YPO_4 \cdot 0.8H_2O$ nanocrystals with and without the Cit^{3-} were performed (Fig. 5). It can be observed that the luminescent $YPO_4 \cdot 0.8H_2O$ sample (Fig. 5(a)) showed two obvious EPR signals at $g = 2.0000$ and $g = 2.0066$ but the $YPO_4 \cdot 0.8H_2O$ sample prepared without Cit^{3-} exhibited no EPR signal in Fig. 5(b). This indicated that the paramagnetic defects related to the luminescence property existed in the luminescent $YPO_4 \cdot 0.8H_2O$ nanocrystals, which was in agreement with the similar result reported by Angelov *et al.*,[31] who found that the $CO_2^{\bullet -}$ radicals exhibiting three EPR signals in the interstitial sites of the aragonite lattice of $SrCO_3$ were most probably responsible for the self-activated luminescence. In addition, Lin Jun and co-workers have reported the luminescence properties of $CO_2^{\bullet -}$ radicals in $Ca_5(PO_4)_3OH$ and $Sr_5(PO_4)_3OH$ host lattice without doping rare earth or transition metal ions as activators.[32,33] Compared with the present work, EPR signal, similar PL results, and together with the synthesis process, we can assume that the luminescence for $YPO_4 \cdot 0.8H_2O$ nanocrystals might be induced by $CO_2^{\bullet -}$ radicals in the $YPO_4 \cdot 0.8H_2O$ host lattice. The $CO_2^{\bullet -}$ radicals might be formed from Cit^{3-} in the hydrothermal process. These radicals may become the optically active centers of self-activated orthophosphate luminescence. In the preparation of orthophosphate samples *via* the hydrothermal process with Cit^{3-}, it is easy to form the metal–citrate complex. Under the high pressure of the thermal process, some of R–C–COO– (Cit^{3-}) undergo cleavages to form R–C (big group) and $CO_2^{\bullet -}$, small amounts of $CO_2^{\bullet -}$ radicals resulting from the bond cleavages are trapped by the already formed orthophosphate lattice or interstitial positions. The residual fragmented bonds ($CO_2^{\bullet -}$) are apparently the precursors for various centers. These defects centers induce an electron to be localized in the 2p orbital of the single bonded carbon. This would give rise to photoluminescence through a strong electron-photon coupling.[34–36] To further confirm the presence of $CO_2^{\bullet -}$ radical impurities, the $YPO_4 \cdot 0.8H_2O$ samples were subjected to FT-IR analysis. The FT-IR spectra for $YPO_4 \cdot 0.8H_2O$ with Cit^{3-} (a) and $YPO_4 \cdot 0.8H_2O$ without Cit^{3-} (b) are shown in Fig. 6. As shown in Fig. 6(a) for the as-prepared $YPO_4 \cdot 0.8H_2O$ sample in the presence of Cit^{3-}, the broad band at 3500 cm^{-1} was attributed to the O–H vibration of H_2O absorbed in the sample. The 1405 and 1618 cm^{-1} peaks were attributed to carbon-related impurities from the addition of Cit^{3-} ions. The band centered at 1010 cm^{-1} was attributed to the asymmetric stretching vibrations of the P–O in PO_4^{3-} groups. The two groups of bands in the low wavenumber ranging from 500 to 680 cm^{-1} (centered at 537, 624 cm^{-1}) were assigned to the bending vibrations of the O–P–O in PO_4^{3-} groups.[37–39] The FT-IR spectrum (Fig. 6(b)) of $YPO_4 \cdot 0.8H_2O$ in the absence of Cit^{3-} in the synthesis process was similar to the spectrum of $YPO_4 \cdot 0.8H_2O$ with Cit^{3-} except for the intensity of the two bands (1405 and 1618 cm^{-1}). The two weak bands can be attributed to very small amount of $CO_2^{\bullet -}$ groups, which might be from CO_2 in aqueous solution or air in the preparation process.[40–42] Through the analysis of the abovementioned experimental results, we can conclude that the radical defects

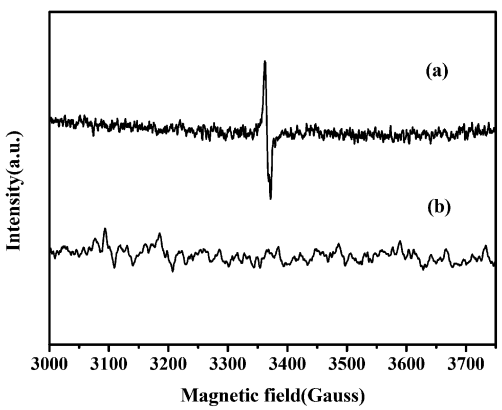

Fig. 5 EPR spectra for (a) luminescent $YPO_4 \cdot 0.8H_2O$ nanocrystals prepared with trisodium citrate and (b) $YPO_4 \cdot 0.8H_2O$ nanocrystals prepared without trisodium citrate.

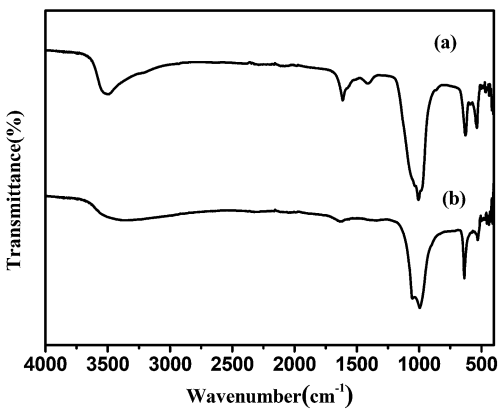

Fig. 6 FT-IR spectra for $YPO_4 \cdot 0.8H_2O$ prepared with trisodium citrate (a), $YPO_4 \cdot 0.8H_2O$ in the absence of trisodium citrate (b).

were induced by Cit^{3-} in the hydrothermal process. The EPR and FT-IR results provided abundant evidence that the carbon-related impurities were induced by Cit^{3-} in the hydrothermal process.

3.3 Photoluminescence properties of $YPO_4 \cdot 0.8H_2O : Tb^{3+}$/ Eu^{3+} nanocrystals

Eu^{3+} ion is a well-known red-emitting activator in commercial phosphors because the emission of the rare earth Eu^{3+} ion consists usually of lines in the red spectral area due to the $^5D_0$–^7F_J ($J = 1, 2, 3, 4, 5$ and 6) transitions. While the Tb^{3+} ion is used as an activator in green phosphors, whose emission is mainly due to the transitions of $^5D_3 \rightarrow {}^7F_J$ in the blue region and $^5D_4 \rightarrow {}^7F_J$ in the green region ($J = 6, 5, 4, 3, 2$), depending on its doping concentration. To show the tunable luminescence, we can co-dope different rare earth ions by varying their concentration. In our experiment, we added Tb^{3+} and Eu^{3+} ions into $YPO_4 \cdot 0.8H_2O$ nanocrystals.

Fig. 7 depicts the excitation and emission spectra of $YPO_4 \cdot 0.8H_2O : 0.04Tb^{3+}$ nanocrystals in the 200–700 nm range. The excitation spectrum (red line) consists of several broad bands. For comparison, the overall excitation spectrum is divided into two parts: one, in the range from 200–290 nm, represents the 4f–5d transition of Tb^{3+}; and the other, in the range from 290–400 nm, represents the 4f–4f transition of Tb^{3+}. The former is assigned to the transitions from the lower energy level of the $4f^8$ configuration to the energy levels of the $4f^7 5d$ configuration of Tb^{3+}, resulting in the direct excitation into Tb^{3+}. For the latter, as expected, this spectral shift is not observed because the 4f shell of Tb^{3+} is well-shielded by 5s and 5p shells, resulting in slight effect of crystal field on energy levels. The characteristic f $\rightarrow$ f transition lines within the Tb^{3+} $4f^8$ configuration in the longer wavelength region are assigned as the transitions from the $^7F_6$ ground state to the different excited states of Tb^{3+}, *i.e.*, 353 nm ($^7F_6 \rightarrow {}^5D_2$), 360 nm ($^7F_6 \rightarrow {}^5L_{10}$), 371 nm ($^7F_6 \rightarrow {}^5G_5$), 379 nm ($^7F_6 \rightarrow {}^5G_6$), respectively.[43–45] Excitation into the $4f^8$–$4f^7 5d$ transition band yields the emission spectrum (black line) that has similar profiles and exhibits four obvious lines centered at 492, 545, 586, and 622 nm, originating from the transitions from the $^5D_4$ excited state to the ^7F_J ($J = 6, 5, 4, 3$) ground states of Tb^{3+} ion, respectively, with $^5D_4 \rightarrow {}^7F_5$ transition at 545 nm as the most prominent group.

In general, the luminescence color of Eu^{3+} ion depends on the host structure, which mainly shows characteristic emissions resulting from the transitions of the $^5D_{0,1,2} \rightarrow {}^7F_J$ ($J = 1, 2, 3, 4$).[46] As shown in Fig. 8, the excitation spectrum monitored with 592 nm consists of two broad excitation bands from 200–340 nm with a maximum at 218 nm, which should be attributed to the host absorption and the charge transfer transition between O^{2-} and Eu^{3+}, respectively.[47] In the longer wavelength region (360–500 nm), Eu^{3+} doped phosphors usually have effective and intrinsic absorption due to the intra-configurational 4f–4f transition of Eu^{3+} at about 395 nm ($^7F_0 \rightarrow {}^5L_6$) and 465 nm ($^7F_0 \rightarrow {}^5D_2$), which make them match well with the near-UV and blue GaN-based LED chips as an efficient red light emitting phosphor. The emission spectrum (Fig. 8, black line) is obtained at 395 nm excitation, which is described by the characteristic emission peaks of Eu^{3+} ions with the transitions from the excited $^5D_0$ state to ^7F_J ($J = 1, 2$) levels at about 592 and 614 nm, respectively. The emission at 592 nm is stronger than that of 614 nm, suggesting a higher occupancy of Eu^{3+} in the asymmetric environment.

3.4 Photoluminescence properties of $YPO_4 \cdot 0.8H_2O : Tb^{3+}$, Eu^{3+} nanocrystals

Energy transfer plays an important role in improving the emission efficiency for solid-state luminescent materials. Because the entire rare earth family is isostructural, it is expected that we can easily tune their emissions by co-doping methods. Among the lanthanide ions, the Eu^{3+} and Tb^{3+} ions are two of the most important luminescent activators, which are attractive in visible luminescent materials due to their strong red and green emissions. Thus, we can co-crystallize them with tunable optical activity.[48,49] In addition, Eu^{3+} and Tb^{3+} have the same charge and similar ionic radii, and hence Eu^{3+} can dope easily into the Tb^{3+} compounds and the corresponding emission color tuning is decided according to the concentration of

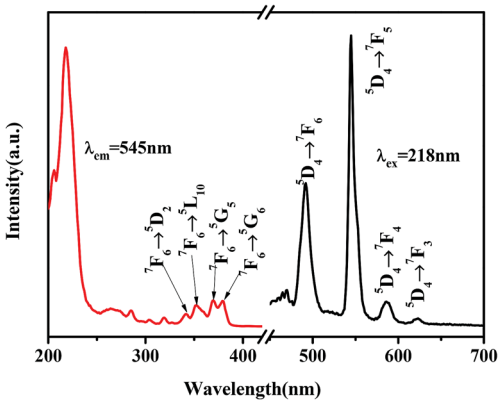

Fig. 7 Excitation ($\lambda_{em} = 545$ nm) and emission ($\lambda_{ex} = 218$ nm) spectra of $YPO_4 \cdot 0.8H_2O : 0.04Tb^{3+}$ nanocrystals at room temperature.

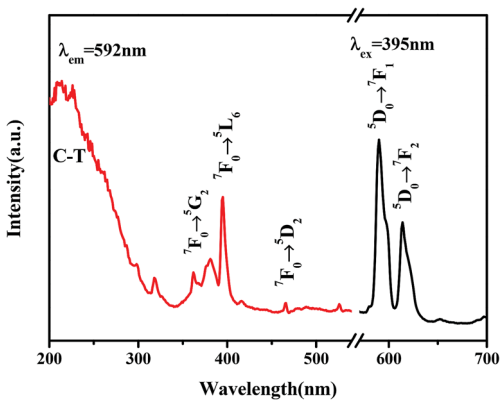

Fig. 8 Excitation ($\lambda_{em} = 592$ nm) and emission ($\lambda_{ex} = 395$ nm) spectra of $YPO_4 \cdot 0.8H_2O : 0.04Eu^{3+}$ nanocrystals at room temperature.

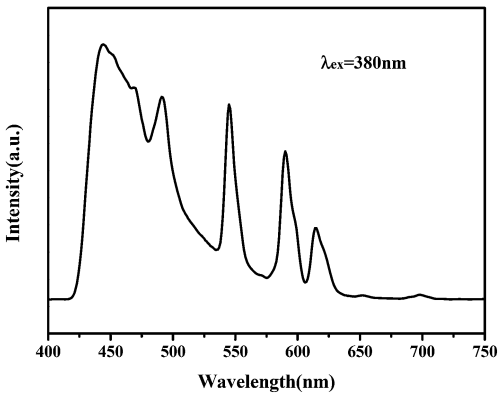

Fig. 9 The emission (λ_{ex} = 380 nm) spectrum of $Y_{0.90}PO_4 \cdot 0.8H_2O$: $0.04Tb^{3+}$, $0.06Eu^{3+}$ nanocrystals at room temperature.

Eu^{3+} ions through the energy-transfer process.[50] Therefore, Tb^{3+} and Eu^{3+} ions co-doped $YPO_4 \cdot 0.8H_2O$ nanocrystals were also prepared in our work, and the emission spectrum of $YPO_4 \cdot 0.8H_2O$: $0.04Tb^{3+}$, $0.06Eu^{3+}$ nanocrystals is shown in Fig. 9. Under the excitation at 380 nm, the red (614 nm, Eu^{3+}), green (545 nm, Tb^{3+}) and blue (494 nm, Tb^{3+}) emission bands can be excited concurrently besides defects/impurities broad band luminescence in the host. In addition, it can also be seen in Fig. 10 that there is overlapping between the emission spectrum of Tb^{3+} and the excitation spectrum of Eu^{3+}. Therefore, we can speculate that energy transfer occurs among Tb^{3+} and Eu^{3+} ions in the $YPO_4 \cdot 0.8H_2O$ nanocrystals.[51–53] In addition, when exciting with 486 nm laser light corresponding to Tb^{3+} : $^7F_6 \rightarrow {}^5D_4$ *transition* (Fig. 11), it can be observed that the emission spectrum (red line) simultaneously contains the 596 nm ($^5D_0 \rightarrow {}^7F_1$) and 618 nm ($^5D_0 \rightarrow {}^7F_2$) of Eu^{3+} and the 549 nm ($^5D_4 \rightarrow {}^7F_5$) transition of Tb^{3+} in $YPO_4 \cdot 0.8H_2O$: $0.04Tb^{3+}$, $0.04Eu^{3+}$ nanocrystals, and the emission intensity of Tb^{3+} $^5D_4 \rightarrow {}^7F_5$ transition clearly decreases compared with that of Tb^{3+} $^5D_4 \rightarrow {}^7F_5$ transition in single $0.04Tb^{3+}$-doped $YPO_4 \cdot 0.8H_2O$ and $YPO_4 \cdot 0.8H_2O$: $0.04Tb^{3+}$, $0.02Eu^{3+}$ samples. Moreover, the emission intensity of Eu^{3+} $^5D_0 \rightarrow {}^7F_2$ and $^5D_0 \rightarrow {}^7F_4$ transitions

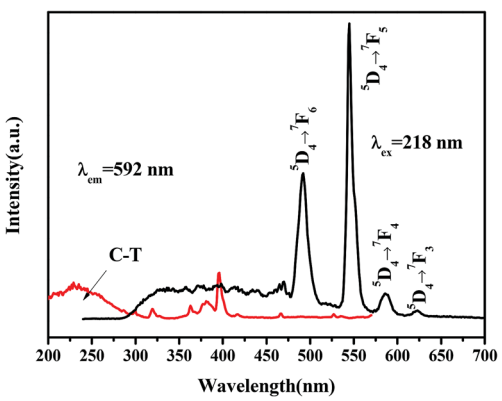

Fig. 10 Emission spectrum of $Y_{0.96}PO_4 \cdot 0.8H_2O$: $0.04Tb^{3+}$ (the black line, λ_{ex} = 218 nm) and the excitation spectrum of $Y_{0.96}PO_4 \cdot 0.8H_2O$: $0.04Eu^{3+}$ (the red line, λ_{em} = 592 nm).

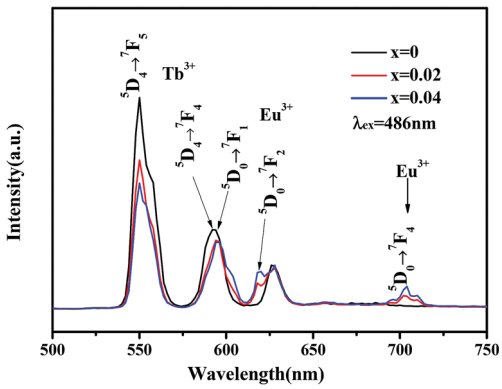

Fig. 11 Emission spectra of $Y_{0.96}PO_4 \cdot 0.8H_2O$: $0.04Tb^{3+}$ (black line), $Y_{0.94}PO_4 \cdot 0.8H_2O$: $0.04Tb^{3+}$, $0.02Eu^{3+}$ (red line) and $Y_{0.92}PO_4 \cdot 0.8H_2O$: $0.04Tb^{3+}$, $0.04Eu^{3+}$ (blue line) nanocrystals under excitation at 486 nm laser light.

in $YPO_4 \cdot 0.8H_2O$: $0.04Tb^{3+}$, $0.04Eu^{3+}$ obviously increases compared with that in $YPO_4 \cdot 0.8H_2O$: $0.04Tb^{3+}$, $0.02Eu^{3+}$ samples. All the spectral results illustrate that Tb^{3+} ions may act as an energy donor in the $YPO_4 \cdot 0.8H_2O$ host, in which excitation energy could be transferred to an acceptor Eu^{3+}.

3.5 Energy transfer and luminescence mechanism in $YPO_4 \cdot 0.8H_2O$: Tb^{3+}, Eu^{3+} nanocrystals

Furthermore, to explore the possibility of energy transfer and realize multicolor tunable luminescence, Fig. 12 shows the variation in PL spectra and emission intensity of $YPO_4 \cdot 0.8H_2O$: $0.04Tb^{3+}$, xEu^{3+} nanocrystals with the increase in Eu^{3+}-doping concentrations from 0 to 0.18. The sample (x = 0) exhibits the typical emission of Tb^{3+} and is characterized by strong bands at ~545 nm ($^5D_4 \rightarrow {}^7F_3$ transition, green emission) and ~491 nm ($^5D_4 \rightarrow {}^7F_4$ transition, blue emission). Although the concentration of Tb^{3+} was fixed, the emission intensity of Tb^{3+} decreased with increasing Eu^{3+} concentration. While the emission intensity of Eu^{3+} first increases with increasing concentration (x), reaches the maximum at x = 0.06, and then decreases with further increasing (x) due to the

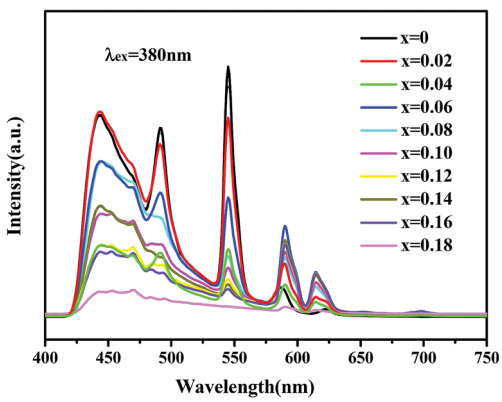

Fig. 12 Emission spectra of $Y_{0.96-x}PO_4 \cdot 0.8H_2O$: $0.04Tb^{3+}$, xEu^{3+} (λ_{ex} = 380 nm) nanocrystals with different Eu^{3+} concentrations.

concentration quenching effect. In many cases, concentration quenching is because of energy transfer from one activator to another until an energy sink in the lattice is achieved. In the energy migration process, the excitation energy will be lost at a killer or quenching site, resulting in the decrease of luminescence intensity. Moreover, because the ion radius of Eu^{3+} and Y^{3+} are different, the crystal structure distortion becomes more serious with an increase in Eu^{3+} doping concentration, which would quench luminescence. However, the luminescence intensity of the Eu^{3+} ions is not as expected, and we speculate that there may be energy transfer between the host and the Eu^{3+} ions. After that, we conducted a series of experiments by doping different rare earth ions, the spectral results are shown in Fig. S1,† which reveal that the change in luminescent intensity could be related to the type of the rare earth ion. When La^{3+} ions without luminescence are doped in $YPO_4 \cdot 0.8H_2O$ nanocrystals, the intensity of defects/impurities broad band luminescence in the host will be stronger. When Tb^{3+} ions are doped in $YPO_4 \cdot 0.8H_2O$ nanocrystals, the intensity of defects/impurities broad band luminescence remains unchanged. However, the defects luminescence becomes weaker when Eu^{3+} ions are doped. Therefore, it is possible that energy transfer occurs between the defects in the host and the Eu^{3+} ions. Further experiments are undergoing.

To further validate energy transfer from Tb^{3+} to Eu^{3+}, we investigated the decay curve of Tb^{3+}. As described by Blasse,[54] the decay behavior of Tb^{3+} can be expressed as

$$I = I_0 \exp(-t/\tau) \quad (1)$$

where I and I_0 are the luminescence intensities at time t and 0, respectively, and τ is the luminescence lifetime. Fig. 13 shows the decay curves of Tb^{3+} emission in $YPO_4 \cdot 0.8H_2O : 0.04Tb^{3+}$, xEu^{3+} (x = 0, 0.02, 0.04, 0.06, 0.08, 0.10, 0.12, 0.14, 0.16, 0.18) samples. For the $YPO_4 \cdot 0.8H_2O : 0.04Tb^{3+}$, xEu^{3+} samples, the lifetime of Tb^{3+} decreases with increasing Eu^{3+} concentrations, which are 2.89 ms, 1.94 ms, 1.55 ms, 1.12 ms, 0.854 ms, 0.594 ms, 0.355 ms, 0.261 ms, 0.256 ms, 0.165 ms, respectively. The luminescence lifetime of Tb^{3+} decreases with increasing Eu^{3+} concentration, as reported by Zhang *et al.*,[55] Nazarov *et al.*[56] and Mueller *et al.*[57] The diminishing lifetimes further confirmed that energy transfer occurred between Tb^{3+} and Eu^{3+}. In addition, the energy transfer efficiency from Tb^{3+} to Eu^{3+} was also investigated. In general, the energy transfer efficiency from a sensitizer to activator can be expressed as the following equation[58–60]

$$\eta_T = 1 - \frac{\tau_s}{\tau_{s0}} \quad (2)$$

because the energy absorbed by Tb^{3+} transferred to Eu^{3+}, which is a strong evidence for energy transfer from Tb^{3+} to Eu^{3+}, where η_T is the energy transfer efficiency and τ_{s0} and τ_s are the lifetimes of a sensitizer in the absence and presence of an activator, respectively.[61] In the $YPO_4 \cdot 0.8H_2O : 0.04Tb^{3+}$, xEu^{3+} systems, Tb^{3+} is the sensitizer and Eu^{3+} is the activator. According to the abovementioned equation, the maximum energy transfer efficiency is 94.31% for $x = 0.18$, as shown in Fig. 14. These high efficiencies of energy transfer primarily originate from the significant spectral overlap between Tb^{3+} emission bands and Eu^{3+} absorption bands, and the energy transfer may occur easily. It depends on the average distance (R) between the Tb^{3+} donor and Eu^{3+} acceptor ions. Exchange interaction generally requires an overlap of the donor and acceptor orbitals and an R value of less than 0.3–0.4 nm; otherwise, the electric multipolar interaction may dominate.[62]

To examine the nature of energy transfer, the Van Uitert's formula[63,64] can be expressed by:

$$\log\left(\frac{I_0 - I}{I}\right) = \log \beta + \left(\frac{\theta}{3}\right)\log\left(\frac{C_\alpha}{C_0}\right) \quad (3)$$

where I_0 and I are the fluorescence intensity of the donor in the absence and presence of the acceptor, respectively, β is a parameter representing the strength of the multipolar interaction and θ is the separation exponent corresponding to the interaction, C_α is the concentration of the acceptor (Eu^{3+}) and C_0 is the concentration of the acceptor (Eu^{3+}) at which the emission intensity of donor (Tb^{3+}) is quenched to 50% of its

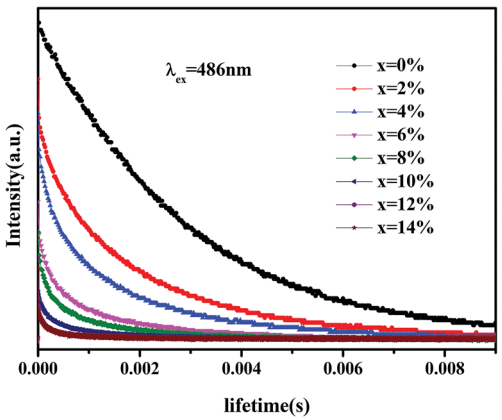

Fig. 13 Decay curve of Tb^{3+} emission transitions in the $Y_{(0.96-x)}PO_4 \cdot 0.8H_2O : 0.04Tb^{3+}$, xEu^{3+} samples (x = 0, 0.02, 0.04, 0.06, 0.08, 0.10, 0.12, 0.14) under excitation at 486 nm laser light.

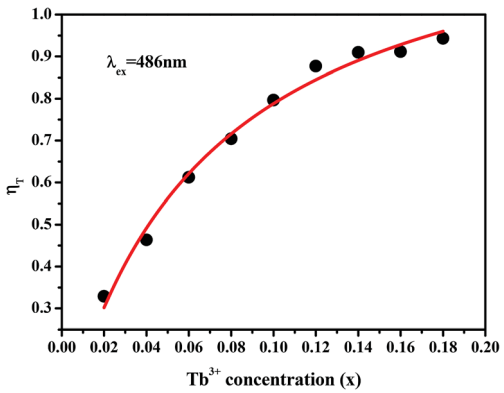

Fig. 14 Energy transfer efficiency Tb^{3+} to Eu^{3+} in $Y_{0.96-x}PO_4 \cdot 0.8H_2O : 0.04Tb^{3+}$, xEu^{3+} samples (x = 0.02, 0.04, 0.06, 0.08, 0.10, 0.12, 0.14, 0.16, 0.18) under excitation at 486 nm laser light.

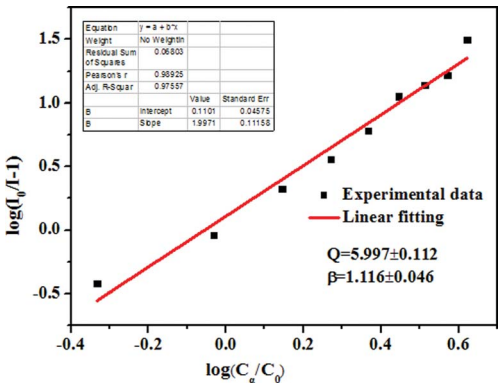

Fig. 15 Plot of intensity variation of Tb^{3+} fluorescence with Eu^{3+} concentration in relation to the Van Uitert's formula.

original value. θ takes the values of 6, 8 or 10 for dipole–dipole, dipole–quadrupole or quadrupole–quadrupole interactions, respectively. We have estimated C_0 to be 4.3 at%, and the corresponding plot is shown in Fig. 15, in which the slope ($\theta/3$) is estimated to be 1.997, suggesting that energy transfer mechanism from the Tb^{3+} to Eu^{3+} ions is an electric dipole–dipole interaction.

Because of energy transfer from Tb^{3+} to Eu^{3+} ions, the relative intensity of the red-light emission of Eu^{3+} gradually increases corresponding to the decrease in the green-emission of Tb^{3+}. The undoped $YPO_4 \cdot 0.8H_2O$ nanocrystals show a strong self-activated blue emission centered at 400 nm, which implies that the emission color can be effectively tuned by controlling Eu concentration. As displayed in Fig. 16, points *a* (0.236, 0.411), *b* (0.234, 0.324), *c* (0.241, 0.252) and *d* (0.269, 0.278) denote the changing trend in the chromatic coordination for different concentrations of Eu^{3+} ions, which can be effectively tuned to white light by changing the Eu^{3+} concentrations. The emission of $YPO_4 \cdot 0.8H_2O : 0.04Tb^{3+}$, xEu^{3+} nanocrystals upon excitation at 380 nm covers the visible-light range with a balance of red (592 nm), green (543 nm) and blue (445 nm) resulting in a white-light emission. This merit of tunable white-light emission gives the materials potential applications in the fields of labeling, sensing, biomedicine, and color display. Moreover, the novel strategy of the combination of self-activated and rare earth ions emissions might serve as a guidance for the design and fabrication of other microscaled inorganic materials with white light emission and tunable luminescent properties.

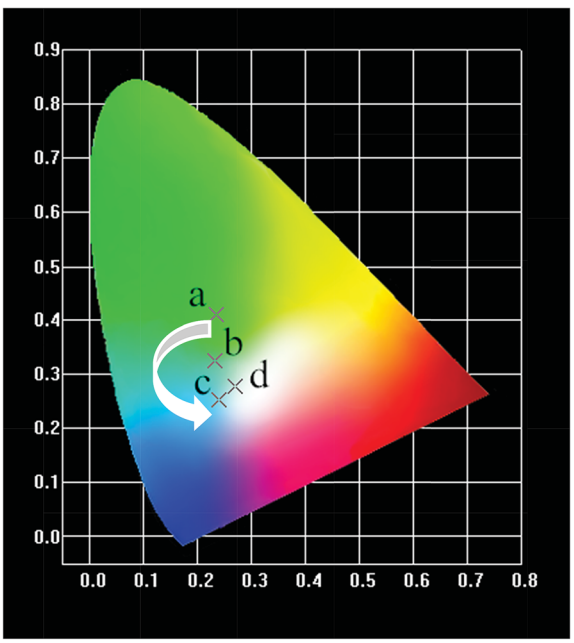

Fig. 16 CIE chromaticity diagram of samples $Y_{0.96-x}PO_4 \cdot 0.8H_2O : 0.04Tb^{3+}$, xEu^{3+} for different concentrations of Eu^{3+} doping: (a) $x = 0$; (b) $x = 0.02$; (c) $x = 0.12$ and (d) $x = 0.18$ under excitation at 380 nm.

4. Conclusions

In conclusion, *via* a simple hydrothermal route, we demonstrated a controlled synthesis of orthophosphate nanocrystals using Cit^{3-} as a "shape modifier". The pH value plays a crucial role in obtaining $YPO_4 \cdot 0.8H_2O$ samples with various morphologies, and a crystallization pH value of 6 was found to be optimal. Meanwhile, a strong blue emission peaking at about 400 nm in $YPO_4 \cdot 0.8H_2O$ nanocrystals was observed at room temperature due to the presence of Cit^{3-}. The $CO_2^{\bullet -}$ radicals in the interstitials of the orthophosphate lattice might be responsible for the self-activated luminescence. Through the analysis of spectra of the $YPO_4 \cdot 0.8H_2O : Tb^{3+}$, Eu^{3+}, there effective energy transfer occurred between Tb^{3+} and Eu^{3+}. Then, by controlling the doping concentration of Eu^{3+}, the luminescent color could be easily modified from green, blue, white due to the different composition of emissions of Eu^{3+} resulting from different energy efficiency at different doping concentrations. Moreover, the energy transfer mechanism was proven to be dipole–dipole interaction. It can be concluded that Cit^{3-} as a template plays an indispensable role in limiting the agglomeration of particles, controlling the size of crystal particles and exhibiting strong blue luminescence of the samples. The suitable excitation wavelength, regular shape and strong luminescence will make $YPO_4 \cdot 0.8H_2O : Tb^{3+}$, Eu^{3+} samples superior candidates in UV LEDs.

Acknowledgements

This work was supported by the Science and Technology Development Planning Project of Jilin Province (20130522173JH), partially sponsored by China Postdoctoral Science Foundation, supported by National Found for Fostering Talents of Basic Science (no. J1103202) and by the Chunmiao Talents of Jilin Province.

References

1 X. F. Li, J. D. Budai, F. Liu, J. Y. Howe, J. H. Zhang, X. J. Wang, Z. J. Gu, C. J. Sun, R. S. Meltzer and Z. W. Pan, *Light: Sci. Appl.*, 2013, **2**, e50–e57.

2 M. M. Shang, G. G. Li, D. L. Geng, D. M. Yang, X. J. Kang, Y. Zhang, H. Z. Lian and J. Lin, *J. Phys. Chem. C*, 2012, **116**, 10222–10231.
3 E. Matioli, S. Brinkley, K. M. Kelchner, Y. L. Hu, S. Nakamura, S. DenBaars, J. Speck and C. Weisbuch, *Light: Sci. Appl.*, 2012, **1**, e22–e28.
4 A. A. Setlur, W. J. Heward, Y. Gao, A. M. Srivastava, R. G. Chandran and R. G. M. V. Shankar, *Chem. Mater.*, 2006, **18**, 3314–3322.
5 J. Limpert, F. Stutzki, F. Jansen, H. J. Otto, T. Eidam, C. Jauregu and A. Tünnermann, *Light: Sci. Appl.*, 2012, **1**, e8–e12.
6 S. X. Yan, J. H. Zhang, X. Zhang, S. Z. Lu, X. G. Ren, Z. G. Nie and X. J. Wang, *J. Phys. Chem. C*, 2007, **111**, 13256–13260.
7 X. F. Fan, W. T. Zheng and D. J. Singh, *Light: Sci. Appl.*, 2014, **3**, e179–e192.
8 L. Manna, E. C. Scher, L. S. Li and A. P. Alivisatos, *J. Am. Chem. Soc.*, 2002, **124**, 7136–7145.
9 X. Wang and Y. D. Li, *Angew. Chem., Int. Ed.*, 2002, **41**, 4790.
10 X. Wang, X. M. Sun, D. P. Yu, B. S. Zou and Y. D. Li, *Adv. Mater.*, 2003, **15**, 1442–1445.
11 X. Wang and Y. D. Li, *Chem.–Eur. J.*, 2003, **9**, 5627–5635.
12 J. X. Zhu, Z. Gui and Y. Y. Ding, *Mater. Lett.*, 2008, **62**, 2373–2376.
13 S. Heer, O. Lehmann, M. Haase and H. U. Gudel, *Angew. Chem., Int. Ed.*, 2003, **42**, 3179–3182.
14 Z. Y. Huo, C. Chen, D. R. Chu, H. H. Li and Y. D. Li, *Chem.–Eur. J.*, 2007, **13**, 7708–7714.
15 H. X. Mai, Y. W. Zhang, L. D. Sun and C. H. Yan, *Chem. Mater.*, 2007, **19**, 4514–4522.
16 R. X. Yan, X. M. Sun, X. Wang, Q. Peng and Y. D. Li, *Chem.–Eur. J.*, 2005, **11**, 2183–2195.
17 Y. P. Fang, A. W. Xu, R. Q. Song, H. X. Zhang, L. P. You, J. C. Yu, *et al.*, *J. Am. Chem. Soc.*, 2003, **125**, 16025–16034.
18 Y. W. Zhang, Z. G. Yan, L. P. You, R. Si and C. H. Yan, *Eur. J. Inorg. Chem.*, 2003, **29**, 4099–4104.
19 L. X. Yu, D. C. Li and M. X. Yue, *Mater. Lett.*, 2007, **61**, 4374–4376.
20 H. Meyssamy, K. Riwotzki, A. Kornowski, S. Naused and M. Haase, *Adv. Mater.*, 1999, **11**, 840–844.
21 N. Banerjee and S. B. Krupanidhi, *Dalton Trans.*, 2010, 9789–9793.
22 J. Q. Hu, Q. Chen, Z. X. Xie, G. B. Han, R. H. Wang, B. Ren, Y. Zhang, Z. L. Yang and Z. Q. Tian, *Adv. Funct. Mater.*, 2004, **14**, 183–189.
23 Z. L. Fu, Z. J. Wu, D. Duan and X. H. Fu, *Dalton Trans.*, 2014, **43**, 2819–2827.
24 Q. Xie, Y. T. Qian, S. Y. Zhang, S. Q. Fu and W. C. Yu, *Eur. J. Inorg. Chem.*, 2006, **2006**, 2454–2459.
25 U. Rambabu, N. R. Munirathnam, T. L. Prakash and S. Buddhudu, *Mater. Chem. Phys.*, 2002, **78**, 160–169.
26 K. Riwotzki, H. Meyssamy, H. Schnablegger, A. Kornowski and M. Haase, *Angew. Chem., Int. Ed.*, 2001, **40**, 573–576.
27 J. B. Liang, J. W. Liu, Q. Xie, S. Bai, W. C. Yu and Y. T. Qian, *J. Phys. Chem. B*, 2005, **109**, 9463–9467.
28 G. Bühler and C. Feldmann, *Angew. Chem., Int. Ed.*, 2006, **45**, 4864–4867.
29 C. M. Zhang, C. X. Li, S. S. Huang, Z. Y. Hou, Z. Y. Cheng, P. P. Yang, C. Peng and J. Lin, *Biomaterials*, 2010, **31**, 3374–3383.
30 C. M. Zhang, S. S. Huang, D. M. Yang, X. J. Kang, M. M. Shang, C. Peng and J. Lin, *J. Mater. Chem.*, 2010, **20**, 6674.
31 S. Angelov, R. Stoyanova, R. Dafinova and K. Kabasanov, *J. Phys. Chem. Solids*, 1986, **47**, 409–412.
32 C. Zhang, J. Yang, Z. Quan, P. Yang, C. Li, Z. Hou and J. Lin, *Cryst. Growth Des.*, 2009, **9**, 2725–2733.
33 C. Zhang, Z. Cheng, P. Yang, Z. Xu, C. Peng, G. Li and J. Lin, *Langmuir*, 2009, **25**, 13591–13598.
34 C. K. Lin, C. M. Zhang and J. Lin, *J. Phys. Chem. C*, 2007, **111**, 3300–3307.
35 B. E. Yoldas, *J. Mater. Res.*, 1990, **5**, 1157–1158.
36 Z. Y. Li, W. M. Lam, C. Yang, B. Xu, G. X. Ni, S. A. Abbah, *et al.*, *Biomaterials*, 2007, **28**, 1452–1460.
37 H. Takeda, Y. Seki, S. Nakamura and K. Yamashita, *J. Mater. Chem.*, 2002, **12**, 2490–2495.
38 A. Doat, M. Fanjul, F. Pelle, E. Hollande and A. Lebugle, *Biomaterials*, 2003, **24**, 3365–3371.
39 L. D. Carlos, R. A. Sá Ferreira, R. N. Pereira, M. Assunc and V. de Zea Bermudez, *J. Phys. Chem. B*, 2004, **108**, 14924–14932.
40 C. M. Zhang and J. Lin, *Chem. Soc. Rev.*, 2012, **41**, 7938–7961.
41 C. M. Zhang, C. K. Lin, C. X. Li, Z. W. Quan, X. M. Liu and J. Lin, *J. Phys. Chem. C*, 2008, **112**, 2183–2192.
42 J. J. J. M. Donners, R. J. M. Nolte and N. A. J. M. Sommerdijk, *Adv. Mater.*, 2003, **15**, 313–316.
43 M. H. Cao, C. W. Hu, Y. H. Wang, Y. H. Guo, C. X. Guo and E. B. Wang, *Chem. Commun.*, 2003, 1884–1885.
44 H. Takeda, Y. Seki, S. Nakamura and K. Yamashita, *J. Mater. Chem.*, 2002, **12**, 2490–2495.
45 C. M. Zhang, Z. Y. Cheng, P. P. Yang, Z. H. Xu, C. Peng, G. G. Li and J. Lin, *Langmuir*, 2009, **25**, 13591–13598.
46 M. Shang, G. Li, X. Kang, D. Yang, D. Geng, C. Peng, Z. Cheng, H. Lian and J. Lin, *Dalton Trans.*, 2012, **41**, 5571–5580.
47 M. Shang, D. Geng, X. Kang, D. Yang, Y. Zhang and J. Lin, *Inorg. Chem.*, 2012, **51**, 11106–11116.
48 J. H. Huang, X. C. Wang, Y. D. Hou, X. F. Chen, L. Wu and X. Z. Fu, *Environ. Sci. Technol.*, 2008, **42**, 7387–7391.
49 J. E. Shelby, *J. Am. Ceram. Soc.*, 1983, **66**, 414–416.
50 Z. J. Zhang, H. H. Chena, X. X. Yang and J. T. Zhao, *Mater. Sci. Eng., B*, 2007, **145**, 34–40.
51 J. Yang, C. M. Zhang, C. X. Li, Y. N. Yu and J. Lin, *Inorg. Chem.*, 2008, **47**, 7262.
52 X. L. Liang, Z. Y. Lin, Y. X. Yang, Z. W. Xing and G. R. Chen, *J. Am. Ceram. Soc.*, 2012, **95**, 275–279.
53 Y. Tian, B. j. Chen, B. N. Tian, N. S. Yu, J. S. Sun, X. P. Li, J. S. Zhang, L. H. Cheng, H. Y. Zhong, Q. Y. Meng and R. N. Hua, *J. Colloid Interface Sci.*, 2013, **393**, 44–52.
54 G. Blasse and B. C. Grabmarier, *Luminescent Materials*, Sprinnger-Verlag, 1994, p. 96.
55 Z. J. Zhang, H. H. Chena, X. X. Yang and J. T. Zhao, *Mater. Sci. Eng., B*, 2007, **145**, 34–40.

56 M. V. Nazarov, D. Y. Jeon, J. H. Kang, E. J. Popovici and L. E. Muresan, *Solid State Commun.*, 2004, **131**, 307–311.
57 A. H. Mueller, M. A. Petruska, M. Achermann, D. J. Werder, E. A. Akhadov, D. D. Koleske, M. A. Hoffbauer and V. I. Klimov, *Nano Lett.*, 2005, **5**, 1039–1044.
58 G. A. Kumar, P. R. Biju, G. Jose and N. V. Unnikrishnan, *Mater. Chem. Phys.*, 1999, **60**, 247–255.
59 P. I. Paulose, G. Jose, V. Thomas, N. V. Unnikrishnan and M. K. R. Warrier, *J. Phys. Chem. Solids*, 2003, **64**, 841–846.
60 S. Rai and S. Hazarika, *Opt. Mater.*, 2008, **30**, 1343–1348.
61 M. M. Shang, G. G. Li, X. J. Kang, D. M. Yang, D. L. Geng and J. Lin, *ACS Appl. Mater. Interfaces*, 2011, **3**, 2738–2746.
62 D. L. Dexter and J. H. Schulman, *Chem. Phys.*, 1954, **22**, 1063–1070.
63 L. G. Van Uitert, *Proc. Int. Conf. Lumin.*, 1966, 1588.
64 L. G. Van Uitert, E. F. Dearborn and J. J. Rubin, *J. Chem. Phys.*, 1966, **45**, 1578–1584.